

## Article

# Reactivity of Rare-Earth Oxides in Anhydrous Imidazolium Acetate Ionic Liquids

Sameera Shah <sup>1,2</sup>, Tobias Pietsch <sup>1,2</sup>, Maria Annette Herz <sup>1</sup>, Franziska Jach <sup>1,2</sup> and Michael Ruck <sup>1,2,\*</sup><sup>1</sup> Faculty of Chemistry and Food Chemistry, Technische Universität Dresden, 01062 Dresden, Germany<sup>2</sup> Max Planck Institute for Chemical Physics of Solids, Nöthnitzer Straße 40, 01187 Dresden, Germany

\* Correspondence: michael.ruck@tu-dresden.de

**Abstract:** Rare-earth metal sesquioxides ( $RE_2O_3$ ) are stable compounds that require high activation energies in solid-state reactions or strong acids for dissolution in aqueous media. Alternatively, dissolution and downstream chemistry of  $RE_2O_3$  have been achieved with ionic liquids (ILs), but typically with additional water. In contrast, the anhydrous IL 1-butyl-3-methylimidazolium acetate [BMIm][OAc] dissolves  $RE_2O_3$  for  $RE = La-Ho$  and forms homoleptic dinuclear metal complexes that crystallize as [BMIm]<sub>2</sub>[RE<sub>2</sub>(OAc)<sub>8</sub>] salts. Chloride ions promote the dissolution without being included in the compounds. Since the lattice energy of  $RE_2O_3$  increases with decreasing size of the  $RE^{3+}$  cation, Ho<sub>2</sub>O<sub>3</sub> dissolves very slowly, while the sesquioxides with even smaller cations appear to be inert under the applied conditions. The Sm and Eu complex salts show blue and red photoluminescence and Van Vleck paramagnetism. The proton source for the dissolution is the imidazolium cation. Abstraction of the acidic proton at the C<sup>2</sup>-atom yields an N-heterocyclic carbene (imidazole-2-ylidene). The IL can be regenerated by subsequent reaction with acetic acid. In the overall process,  $RE_2O_3$  is dissolved by anhydrous acetic acid, a reaction that does not proceed directly.

**Keywords:** anhydrous complexes; dinuclear complexes; ionic liquids; photoluminescence; rare-earth oxides; regeneration; Van Vleck paramagnetism



**Citation:** Shah, S.; Pietsch, T.; Herz, M.A.; Jach, F.; Ruck, M. Reactivity of Rare-Earth Oxides in Anhydrous Imidazolium Acetate Ionic Liquids. *Chemistry* **2023**, *5*, 1378–1394. <https://doi.org/10.3390/chemistry5020094>

Academic Editors: Christoph Janiak, Sascha Rohn and Georg Manolikakes

Received: 31 March 2023

Revised: 19 May 2023

Accepted: 22 May 2023

Published: 2 June 2023



**Copyright:** © 2023 by the authors. Licensee MDPI, Basel, Switzerland. This article is an open access article distributed under the terms and conditions of the Creative Commons Attribution (CC BY) license (<https://creativecommons.org/licenses/by/4.0/>).

## 1. Introduction

Rare earths, such as monazite, bastnasite, loparite and laterite clays, are the natural source of rare-earth elements and their compounds, which are essential, e.g., for luminophores, magnets, catalysts, superconductors, biomedical diagnosis, therapy, and environmental chemistry [1–3]. Although rare-earth elements are not as rare as their name suggests, their extraction is demanding, which has an impact on both price and environment. In the first production step, the phosphate mineral monazite is dissolved either in concentrated H<sub>2</sub>SO<sub>4</sub> at temperatures between 150 and 200 °C (acid process) or in 70% NaOH (basic process) at 140 to 150 °C using autoclaves. After this activation step, an elaborate procedure for the separation of the different metal species follows. Nowadays, the recycling of industrial and electronic waste has also become an important source of rare-earth metals. In many of these processes, rare-earth metal oxides occur as intermediate or final products. For any downstream chemistry, high temperatures or aggressive chemicals must again activate these stable oxides.

With the goal of establishing a more sustainable process, much research has been done in recent years on the chemistry of rare-earth compounds in ionic liquids (ILs) [4–9]. In most investigations, the focus lies on the development of new liquid extraction and separation techniques. Unfortunately, most ILs successfully tested for this purpose have severe weaknesses. First-generation ILs, such as [BMIm]Cl·*n*AlCl<sub>3</sub> ([BMIm]<sup>+</sup> = 1-*n*-butyl-3-methylimidazolium), are sensitive to air and moisture, which strongly limits their usefulness [10]. Super-acidic ILs combined with a stream of chlorine gas also dissolve rare-earth oxides [11]; however, using a highly toxic gas does not achieve the

aim of green chemistry. Nevertheless, there are also some existing reports on the direct dissolution of rare-earth oxides in ILs [12–17]. Water-stable ILs containing Brønsted acidic groups, in particular the very effective IL [Hbet][NTf<sub>2</sub>] ([Hbet]<sup>+</sup> = betainium, [NTf<sub>2</sub>]<sup>−</sup> = bis(trifluoromethylsulfonyl)imide), are much more suitable. Its excellent dissolution power for metal oxides is based on the acidity of the [Hbet]<sup>+</sup> cation and the complexation capacity of the conjugate base (bet) [18]. The weakly coordinating anion [NTf<sub>2</sub>]<sup>−</sup>, however, is expensive and ecologically questionable [19]. Moreover, these IL-based approaches typically involve water as a co-solvent. However, water narrows the electrochemical window and can have a detrimental effect on the subsequent chemistry.

In this work, we show that the anhydrous IL 1-butyl-3-methylimidazolium acetate [BMIm][OAc] can dissolve rare-earth oxides. Acetate, [OAc]<sup>−</sup>, is much cheaper than [NTf<sub>2</sub>]<sup>−</sup> and ecologically harmless. Moreover, it has a complexing effect. Similarly, the nitrogen atoms in the positions 1 and 3 of the imidazole ring can form N-donor coordination complexes [20]. The proton at the C<sup>2</sup>-position of the ring is acidic and can be abstracted by a base. This generates an N-heterocyclic carbene (imidazole-2-ylidene), which can be functional in organo-catalytic reactions [21,22]. Imidazolium acetate ILs have been used to dissolve biomass, e.g., cellulose, and to store CO<sub>2</sub> [23–26].

It is known that traces of chloride, which is a strong nucleophile in most ILs, facilitate the dissolution of metal oxides [27,28] but also of covalently bonded substances such as red phosphorus [29–31]. We have also applied this here and succeeded in establishing an effective and inexpensive method for the chemical activation of RE<sub>2</sub>O<sub>3</sub> (RE = La–Ho, except the radioactive Pm) at moderate temperature, including the recycling of the IL. In addition, we crystallized anhydrous, homoleptic, dinuclear rare-earth metal complexes from these solutions and studied the magnetic and luminescence properties of the Eu and Sm complexes, which were previously synthesized from expensive anhydrous rare-earth metal trihalides [32].

## 2. Materials and Methods

**Chemicals.** The ionic liquids 1-butyl-3-methylimidazolium acetate [BMIm][OAc] (98%), 1-butyl-2,3-dimethylimidazolium chloride [BDMI]Cl, and 1-butyl-3-methylimidazolium chloride [BMIm]Cl (99%) were purchased from Iolitec (ionic liquids technology GmbH (Heilbronn, Germany)). Potassium acetate (99.9%) was purchased from Merck (Darmstadt, Germany). [BDMI][OAc] was synthesized from [BDMI]Cl and potassium acetate in ethanol following a literature procedure for the production of [BMIm][OAc] [33]. All ILs were dried at 110 °C under dynamic vacuum (Schlenk line) overnight and transferred to the glove box before use. HPLC grade ethanol and acetonitrile were obtained from Merck (Darmstadt, Germany). Acetic acid (100%) was obtained from Carl Roth (Karlsruhe, Germany). Ce<sub>2</sub>O<sub>3</sub> was synthesized by heating CeO<sub>2</sub> and Ce to 1500 °C for 24 h in a sealed tantalum ampule [34]. The other rare-earth oxides (99.9%) were obtained from Fluka Chemie GmbH (Buchs, Switzerland).

**Synthesis of [BDMI][OAc].** [BDMI][OAc] was synthesized by mixing 20 mmol (3.75 g) of [BDMI]Cl in 10 mL anhydrous ethanol with 50 mL of an ethanolic solution of 4.8 g potassium acetate under vigorous stirring at room temperature [33]. KCl precipitated quickly, but the solution remained in the stirring bath overnight at room temperature for a complete reaction. KCl was removed via vacuum filtration, and the resultant filtrate was dried in a rotatory evaporator at 70 °C under reduced pressure. Post-precipitation of potassium acetate required additional vacuum filtration. The resulting pale yellow liquid was dried under dynamic vacuum (Schlenk line) at 110 °C overnight.

**Synthesis of [BMIm]<sub>2</sub>[RE<sub>2</sub>(OAc)<sub>8</sub>].** For RE = La–Eu, 1 mmol of RE<sub>2</sub>O<sub>3</sub> powder was mixed with 10 mmol of [BMIm][OAc] and 1 mmol of [BMIm]Cl in a round bottom flask with magnetic stirring at 175 °C. For RE = Gd–Ho, the amount of [BMIm]Cl was increased to 5 mmol and 175 °C was applied for 48 h. After cooling the solutions to room temperature, platelet-shaped crystals of the complex salts [BMIm]<sub>2</sub>[RE<sub>2</sub>(OAc)<sub>8</sub>]

precipitated within few days. The crystals were separated by centrifugation and washed several times with acetonitrile.

*Regeneration of [BMIm][OAc].* After separation of the  $[\text{BMIm}]_2[\text{RE}_2(\text{OAc})_8]$  precipitate, the reacted IL contained a large portion of imidazole-2-ylidene, residuals of the dissolved complex as well as acetonitrile from the washing procedure. The IL was regenerated by mixing with a  $2 \text{ mol L}^{-1}$  solution of acetic acid in acetonitrile at room temperature under inert conditions. A white precipitate formed, which was centrifuged, and the supernatant liquid phase was pipetted off. Acetonitrile and excess acetic acid were evaporated off from the organic phase, first at  $70 \text{ }^\circ\text{C}$  using a rotatory evaporator for 3 h and then at  $100 \text{ }^\circ\text{C}$  on a Schlenk line under dynamic vacuum overnight.

*Powder X-ray Diffraction.* PXRD data were collected on an Empyrean diffractometer PANalytical (Malvern, Worcestershire, UK) equipped with a curved Ge(111)-monochromator in Bragg-Brentano geometry at 296 K using  $\text{Cu-K}\alpha_1$  radiation ( $\lambda = 1.54056 \text{ \AA}$ ). The data were collected in reflection mode in the range  $5^\circ \leq 2\theta \leq 90^\circ$ , with a step width of  $\Delta(2\theta) = 0.01^\circ$ .

*Single-Crystal Structure Determination.* Single-crystal X-ray diffraction data were collected on a four-circle Kappa APEX II CCD diffractometer (Bruker, Madison, WI, USA) with a graphite(002)-monochromator and a CCD detector using  $\text{Mo-K}\alpha$  radiation ( $\lambda = 0.71073 \text{ \AA}$ ) under flowing nitrogen gas at  $T = 100 (2) \text{ K}$ . The data were corrected for background, Lorentz factor, and polarization factor using the APEX III software. Empirical multi-scan absorption correction was applied [35,36]. The structures were solved using SHELXT in OLEX2 [37,38]. SHELXL was used for refinement against  $F^2$  [39,40]. Anisotropic displacement parameters were refined for all non-hydrogen atoms. H atoms were refined without constraints. The structure was visualized with the Diamond software Version 4.6.8 (Klaus Brandenburg, Bonn, Germany) [41].

*NMR Spectroscopy.* The samples were dissolved in deuterated DMSO- $d_6$  and filled in an NMR tube. Measurements were performed on a Bruker Avance (Leipzig, Germany) Neo WB 300 MHz NMR spectrometer at resonance frequencies of 300 MHz for  $^1\text{H}$  and 75.5 MHz for  $^{13}\text{C}$  spectra. The chemical shifts were referenced externally according to tetramethylsilane (TMS) and were calibrated with 10% ethylbenzene in  $\text{CDCl}_3$  as external reference. The signals in the spectra were assigned with the NMR Predictor from ACD/Labs [42].

*UV-Vis Spectroscopy.* The sample was a powder consisting of 10 mg of the complex salt and 100 mg of  $\text{BaSO}_4$ . The spectra were recorded with a solid-state UV-Vis spectrophotometer Varian-4000 (Varian BV, Middelburg, The Netherlands).

*Emission Spectroscopy.* Photoluminescence of powder samples was measured on a spectrofluorometer Fluoro Max-4r (Horiba scientific, Piscataway, NJ, USA). The light source was a xenon arc lamp with photomultiplier R928P detector.

*IR Spectroscopy.* FTIR spectra of liquid samples soon after dissolution (no visible precipitates) as well as a crystal of  $[\text{BMIm}]_2[\text{Eu}_2(\text{OAc})_8]$  were measured on a Bruker Vertex 70 FTIR spectrophotometer (Bruker Optics GmbH, Ettlingen, Germany) with attenuated total reflection (ATR) accessory in the range from 500 to  $4000 \text{ cm}^{-1}$ , with 32 scans per measurement. The data were analyzed using the OPUS 6.5 software (Bruker, Ettlingen, Germany) [43].

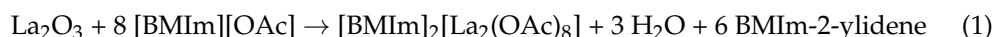
*Thermogravimetric Analysis (TGA) and Differential Scanning Calorimeter (DSC).* The thermal stability of several complex salts was investigated with TGA using an STA 409 Luxx (Netzsch, Selb, Germany). The TGA experiments were carried out in the temperature range from 25 to  $500 \text{ }^\circ\text{C}$ , with a heating rate of  $5 \text{ K min}^{-1}$  in an argon stream. The thermal effects upon heating with  $5 \text{ K min}^{-1}$  in an argon stream were determined using a DSC1 (Mettler Toledo GmbH, Giessen, Germany).

*Magnetic Measurement.* The magnetic susceptibility of the Sm and Eu complex salts were measured with helium-cooled mini-CFMS (Cryogenic, The Vale London, UK) equipped with a vibrating-sample magnetometer (VSM, The Vale London, UK) in the temperature range from 300 K to 2 K.

### 3. Results and Discussion

#### 3.1. Dissolution of $RE_2O_3$

In orienting experiments, we tested the dissolution of the comparatively inexpensive  $La_2O_3$  in seven phosphonium- or imidazolium-based ILs at 175 °C in closed flasks under argon (Table S1). Only in the case of [BMIm][OAc] was no solid residue found after 48 h. Droplets of water condensed in the upper, colder part of the flask. After cooling the solution to room temperature, the complex compound  $[BMIm]_2[La_2(OAc)_8]$  crystallized within some days (see below). The only hydrogen source for the formation of water in this system is the acidic proton at the C<sup>2</sup> atom of the imidazolium cation. In fact,  $La_2O_3$  did not dissolve in 1-butyl-2,3-dimethyl imidazolium acetate, [BDMIm][OAc], which is methylated at the C<sup>2</sup>-position and thus has no acidic proton. The reaction is summarized in Equation (1):



The deprotonated [BMIm]<sup>+</sup> cation is a N-heterocyclic carbene (imidazole-2-ylidene). This is sensitive to air at the reaction temperature, which leads to decomposition when the reaction is performed in a system open to the atmosphere. However, at room temperature the reactivity of the carbene is strongly reduced, allowing handling of the solution and separation of the solid product in air.

It is known that the basic acetate ion can abstract the acidic proton from the [BMIm]<sup>+</sup> cation and form acetic acid [44,45]. Remarkably,  $La_2O_3$  did not dissolve in neat acetic acid (100%) at 175 °C under argon. However, when  $La_2O_3$  was mixed with [BDMIm][OAc] and acetic acid, a vigorous reaction occurred already at room temperature, resulting in a white microcrystalline precipitate of a lanthanum complex that was soluble in water, partially soluble in ethanol, and insoluble in acetone (for PXRD see Figure S1). Obviously, the cation of the IL is necessary for the dissolution; through this, there is enough free acetate in the solution for the formation of the acetate complex, and a stable salt can be precipitated.

According to Equation (1), the molar ratio of  $RE_2O_3$  and [BMIm][OAc] must be at least 1:8. Since the IL is not only a reactant but also the solvent, an excess is advisable to avoid overly high viscosity. To still obtain fairly concentrated solutions, we kept the ratio of 1:10 for the subsequent experiments with  $RE_2O_3$ . In view of the catalytic effect of chloride on the dissolution of many metal oxides in ILs, we also repeated the dissolution experiments with admixtures of [BMIm]Cl in diverse molar ratios as the chloride source. A summary of the dissolution experiments performed can be found in Table S2.

Achieving complete dissolution below 150 °C proved difficult, as the viscosity increased with decreasing temperature, which affected the diffusion and wetting behavior of the IL. In addition, below 120 °C, abstraction of the proton from the substituted imidazolium cations was hindered [44].

The lighter  $RE_2O_3$  ( $RE = La-Nd$ ) dissolved completely, also without the addition of chloride. However, chloride shortened the reaction time and the quality of the crystals was improved (Figure S2), although chloride is not a component of the complex salt. For  $RE = Dy-Ho$ , the dissolution took much more time, especially without chloride.  $RE_2O_3$  with  $RE = Er-Lu, Sc, \text{ or } Y$  did not react with [BMIm][OAc], even when the reaction time, the temperature, or the concentration of the IL was increased or chloride had been added (Figure 1). Instead, decomposition of the IL was observed.

Such a dissolution behavior is well known and understood. In the series of  $RE^{3+}$  cations, the effective ionic radius (for coordination number 9) decreases from 1.216 Å ( $La^{3+}$ ) to 1.032 Å ( $Lu^{3+}$ ) [46]. The smaller the  $RE^{3+}$  cation, the shorter the cation–anion distance, the higher the lattice energy, and the poorer the solubility of the  $RE_2O_3$ . In the underlying case, the boundary is between 1.08 and 1.07 Å, with Ho (1.072 Å) showing poor solubility and Y (1.075 Å) and Er (1.062 Å) apparently none.  $CeO_2$ , which has a much high lattice energy due to the higher cation charge, did not dissolve at all.

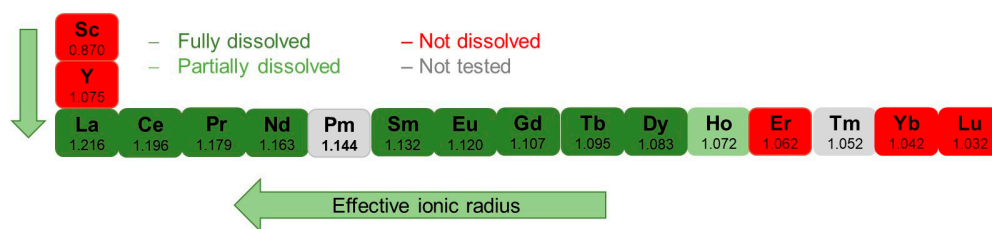


**Figure 1.** Qualitative solubility of  $RE_2O_3$  in [BMIm][OAc] or mixtures of [BMIm][OAc] with [BMIm]Cl. The effective ionic radii of the  $RE^{3+}$  cations for CN 9 are given in Å [46].

This behavior can be used for the separation of rare-earth elements. The four equimolar mixtures  $La_2O_3/Sc_2O_3$ ,  $La_2O_3/Lu_2O_3$ ,  $Eu_2O_3/Y_2O_3$ , and  $Eu_2O_3/CeO_2$  were treated at 175 °C in an IL consisting of [BMIm][OAc] and [BMIm]Cl (molar ratio of 10:1) for few hours. The unreacted solid was separated from the liquid, washed three times with acetonitrile, weighted, and analyzed with PXRD. In all cases, the diffraction patterns showed no evidence of the soluble oxide (Figure S3), and the weight of the recovered insoluble oxide was within 1% of the original. From the separated solutions, the [BMIm]<sub>2</sub>[RE<sub>2</sub>(OAc)<sub>8</sub>] salts ( $RE = La, Eu$ ) precipitated.

### 3.2. Regeneration of the Reacted Ionic Liquid

Under prolonged thermal stress, the dialkylimidazolium cations of the corresponding acetate ILs decompose into alkylated anions and imidazole derivatives [25,47–49] (see also Section 3.4). The decomposition is the reverse reaction of the quaternization (reversed Menshutkin-like reaction). Further decomposition products result from the deprotonation of the C<sup>2</sup>-atom of the imidazolium ring by strong nucleophiles [50], as the resulting N-heterocyclic carbene reacts either with the IL or with other decomposition products [51]. However, the carbene formation is reversible, and the IL can be regenerated by the addition of acid. Irreversible decomposition of the IL can be largely avoided by heating at moderate temperature and for only short periods of time.

The regeneration of used [BMIm][OAc] (Figure S4) was done by reaction with a solution of acetic acid in acetonitrile at room temperature under inert conditions. After evaporation of the acetonitrile and excess acetic acid, the recovered IL was analyzed spectroscopically. The FTIR spectra of neat and regenerated IL are almost identical (Figure S5). In the <sup>13</sup>C and <sup>1</sup>H NMR spectra (Figure 2), no residual acetic acid and acetonitrile was found in the regenerated IL. Generally, the proton signal of acetic acid lies between 10 and 15 ppm, and that of acetonitrile near 2 ppm [52,53]. The decomposition products methyl acetate and 1-butylimidazole were also not detected. While the ester was likely cleaved in the treatment, the alkylimidazole likely precipitated as a coordination compound (white precipitate, see Materials and Methods).

No solid residue remained after combustion of the regenerated IL in air. The <sup>13</sup>C NMR spectra of regenerated and neat IL showed no difference as long as the freshly regenerated IL was stored under inert conditions (sample A). After some time in air (sample B), the <sup>1</sup>H NMR spectrum of the regenerated IL showed a broad resonance signal at 5 ppm, which can be attributed to H<sub>2</sub>O, and also an up-field shift of the protons at C<sup>2</sup>, C<sup>4</sup>, and C<sup>5</sup>. The same effect was observed when water was added to the freshly regenerated IL (Figure S6) as has been reported previously [54,55]. The new signals marked with asterisks in the spectra of (B) indicate a decomposition product. This is probably due to the small amount of carbene that is formed by the internal acid–base equilibrium between [BMIm]<sup>+</sup> and [OAc]<sup>−</sup> (Section 3.4).

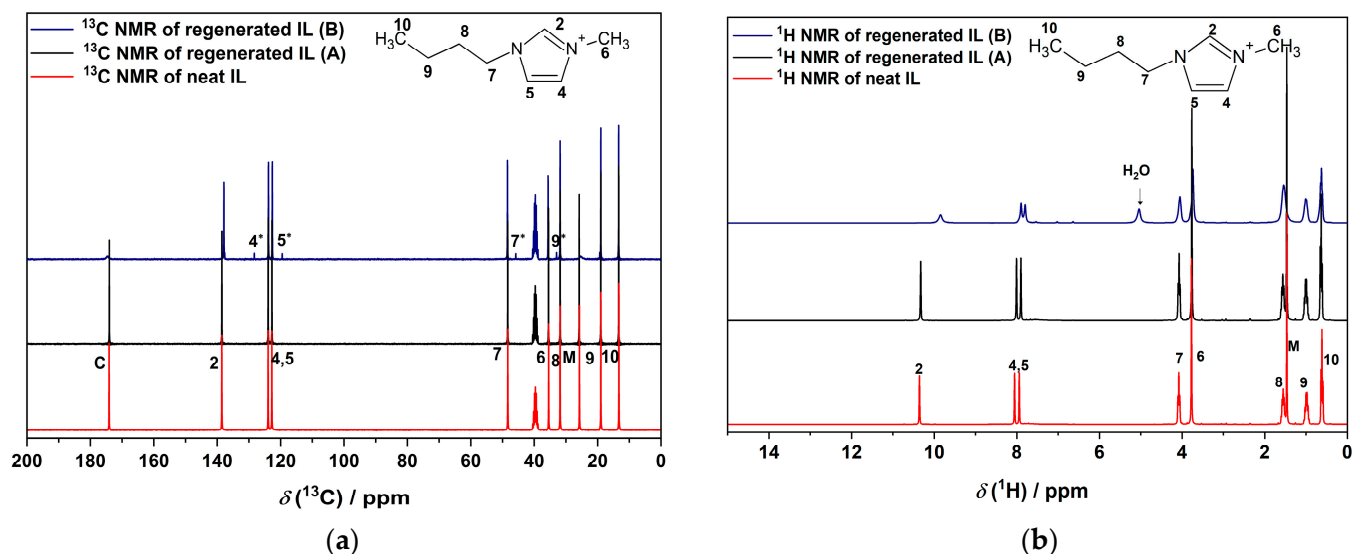


**Figure 2.** (a) <sup>13</sup>C and (b) <sup>1</sup>H NMR spectra of neat [BMIm][OAc] and the regenerated IL. The regenerated IL was stored under inert conditions (A) or in air (B). The signals of [BMIm]<sup>+</sup> are assigned to the atoms at the marked positions in the structures above [26]. M and C represent the methyl and carboxylic groups of acetate. The asterisk sign \* indicates the decomposition product in regenerated IL in air (B). Deuterated DMSO-d<sub>6</sub> was used for diluting all samples.

### 3.3. [BMIm]<sub>2</sub>[RE<sub>2</sub>(OAc)<sub>8</sub>] Complex Salts

After one to four days at room temperature, salts of homoleptic dinuclear rare-earth metal complexes [BMIm]<sub>2</sub>[RE<sub>2</sub>(OAc)<sub>8</sub>] (RE = La–Pr, Nd, Sm–Ho) crystallized from the RE<sub>2</sub>O<sub>3</sub> solutions in [BMIm][OAc] (with or without chloride). The yields were between 25 and 84% (Table S2). The powder X-ray diffractogram of [BMIm]<sub>2</sub>[Eu<sub>2</sub>(OAc)<sub>8</sub>] confirms a single-phase product (Figure S7).

Unlike many other complexes obtained from RE<sub>2</sub>O<sub>3</sub> and ILs, these are anhydrous compounds. Up to now, such anhydrous complexes were made from anhydrous chlorides, nitrates, or acetates, i.e., starting materials that must be synthesized and are much more expensive than the oxides [56–58].

The washed crystals of [BMIm]<sub>2</sub>[RE<sub>2</sub>(OAc)<sub>8</sub>] are air-stable (thick) platelets and appear colorless, except the light-green Pr salt. In the case of the Pr and Dy compounds, the platelet-shaped crystals transformed into thin needles within a day when stored in the reacted IL in air at 10 °C (Figure S8). The powder diffractogram and the IR spectra of the platelets and the needles clearly differ (Figures S9 and S10). Subsequently, the needles turned into yellowish translucent flakes that decompose into dark brown microscale needles within several days.

The structure of plate-like crystals was determined with single-crystal X-ray diffraction (Table S3). As the sum formula suggests, the compounds consist of [BMIm]<sup>+</sup> cations and negatively charged [RE<sub>2</sub>(OAc)<sub>8</sub>]<sup>2−</sup> complexes. Nine oxygen atoms of acetate anions coordinate each RE<sup>3+</sup> cation in the shape of a distorted tricapped trigonal prism (Figure 3). The RE–O bond length develops according to the effective radii of the RE<sup>3+</sup> cations (Table S4). The carboxylate groups of the acetate anions coordinate in three different modes (Figure 4). The two RE<sup>3+</sup> anions are connected through four carboxylate groups.

The salts [BMIm]<sub>2</sub>[RE<sub>2</sub>(OAc)<sub>8</sub>] adopt two different types of crystal structure, depending on the size of the rare-earth (RE) cation. Both structure types have triclinic symmetry (space group type *P*1) and contain two formula units in the unit cell; however, their lattice translations are very different. Bond lengths (Table S5) and the basic arrangements of the molecules are similar in the two structure types, but they differ in translational and molecular point symmetry. Figure S11 shows analogous subcells of the two structure types, reduced to the RE<sup>3+</sup> cations. Their positions relative to the

locations of the inversion centers differ in the two cases. Translational pseudosymmetry is observed (*B*-centering for  $RE = \text{La–Pr}$  and *A*-centering for  $RE = \text{Nd–Ho}$ ). Yet, there are clear superstructure reflections that corroborate the primitive Bravais lattices.

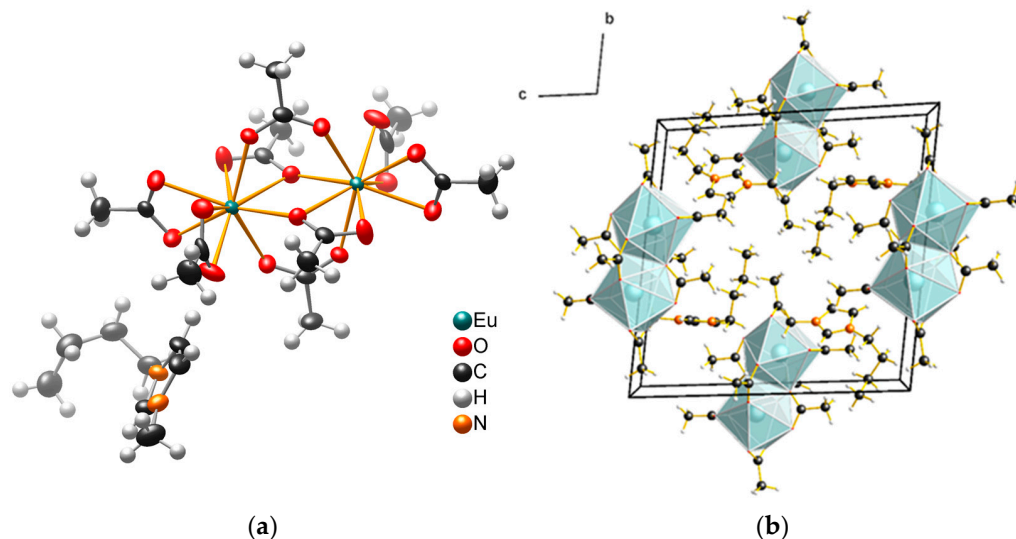


**Figure 3.** (a) Molecular and (b) crystal structure of  $[\text{BMIm}]_2[\text{Eu}_2(\text{OAc})_8]$ . The ellipsoids (in (a)) enclose a space in which with 90% probability the electron density of the atoms can be found at 100 K.

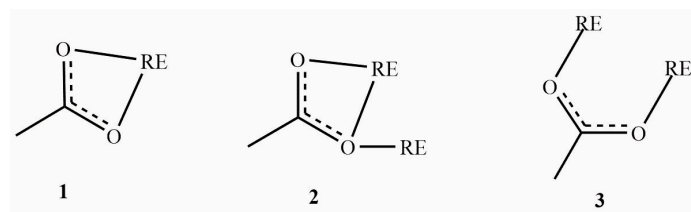


**Figure 4.** Coordination modes of acetate ions in the  $[\text{BMIm}]_2[\text{RE}_2(\text{OAc})_8]$  complexes. (1) Chelating ( $\eta^2$  mode), (2) chelating, bridging ( $\mu_2-\eta^2: \eta^1$  mode), (3) bridging ( $\mu_2-\eta^1: \eta^1$  mode).  $\eta$  represents the number of coordinating ligand atoms to the metal atom, and  $\mu$  represents the number of metal atoms that are coordinated by the same ligand.

For  $RE = \text{La–Pr}$ , the anionic  $[\text{RE}_2(\text{OAc})_8]^{2-}$  complex is non-centrosymmetric, with two crystallographically independent  $RE$  atoms. However, it has a pseudo-center of inversion. The two crystallographically distinct  $[\text{BMIm}]^+$  cations show a combined disorder. The majority position of one cation is connected to the minority position of the other cation by the pseudo-inversion. The fact that there are two positions for the  $[\text{BMIm}]^+$  cation that can be alternatively occupied without significant impact on the position of the anions suggests that the complexes form a packing that includes larger cavities than needed for the organic cations.

In the second structure type, which is adopted by the compounds  $RE = \text{Nd–Ho}$ , the  $[\text{RE}_2(\text{OAc})_8]^{2-}$  complexes are truly centrosymmetric. The packing is slightly different, and the  $[\text{BMIm}]^+$  cations are ordered. Thus, it could be argued that this packing is more efficient than the first; however, there is no unusual reduction in the volume of the unit cell when changing the structure type from the Pr to the Nd compound.

### 3.4. IR and NMR Spectra

Nockemann et al. showed that dinuclear rare-earth betaine complexes  $[\text{RE}_2(\text{bet})_8(\text{H}_2\text{O})_2]^{6+}$  can dissociate into mononuclear units in ILs [59]. It could therefore be argued that, also in the underlying case, the dissolved species might be mononuclear. Acetates have been studied extensively with vibrational spectroscopy. Among the 15 active infrared frequencies

in acetate ions, the symmetric and asymmetric stretching frequencies of the carboxylic group were analyzed using FTIR spectroscopy. The spectra of various  $RE_2O_3$  dissolved in the IL as well as of crystalline  $[BMIm]_2[Eu_2(OAc)_8]$  show additional bands along with shifted and split bands of the neat IL (Figure 5).

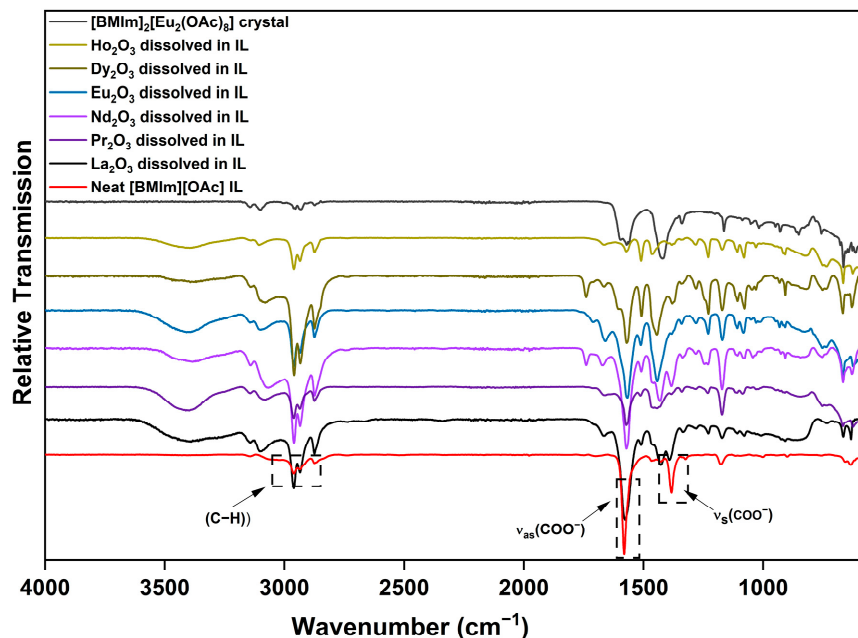


**Figure 5.** FTIR spectra of the  $[BMIm]_2[Eu_2(OAc)_8]$  salt, diverse solutions of  $RE_2O_3$  in  $[BMIm][OAc]$ , and the neat IL.

The C–H stretching frequencies of the organic cation in neat  $[BMIm][OAc]$  lie at about  $3000\text{ cm}^{-1}$ , e.g.,  $\nu_{as}(CH_2) = 2952$ ,  $\nu_{as}(CH_3) = 2932$ , and  $\nu_s(CH_3)$  and  $\nu_s(CH_2) = 2873\text{ cm}^{-1}$ . The asymmetric  $\nu_{as}$  and symmetric  $\nu_s$  stretching frequencies of the carboxylic group are found at  $1575$  and  $1385\text{ cm}^{-1}$  [60]. For the solutions and the complex salt, the signals of the carboxylic group are slightly shifted and split or broadened according to the diverse coordination modes of the acetate ion. Nakamoto et al. showed that the nature of the acetate coordination is related to the difference of  $\nu_{as}-\nu_s$  [61]. Since the diverse signals cannot be reliably assigned to the different coordination modes, further evaluation is not possible. Nonetheless, the differences in the FTIR spectra suggest that the complexes in solution can differ from the crystallized one [62]. The broad bands at about  $3400\text{ cm}^{-1}$  in the spectra of the solutions indicate the water formed during the dissolution of the oxides. When the system was kept open during the reaction, this led to the decomposition of the IL, as shown by the FTIR spectrum in Figure S12.

Using  $^{13}C$  and  $^1H$  NMR spectroscopy (Figure 6), we compared three samples (Figure S4): the unreacted IL, a freshly prepared solution of  $La_2O_3$  in  $[BMIm][OAc]$  from which no precipitation had occurred, and the supernatant of a solution from which the complex salt had precipitated and which had been stored in air for several months. In addition, a dark solution containing decomposition products of  $[BMIm][OAc]$  after heating  $La_2O_3$  in the IL for 4 days at  $175\text{ }^\circ\text{C}$  was investigated (Figure S13).

In the  $^{13}C$  and  $^1H$  NMR spectra of the freshly reacted solution, methyl acetate and 1-butylimidazole are identified as decomposition products known from the literature [25,63,64].  $^{13}C$  NMR-DEPT-135 spectroscopy (DEPT = Distortionless Enhancement by Polarization Transfer; Figure S14) supports the assignment of the signals. The  $^{13}C$  NMR signal of the carboxylic group at  $175\text{ ppm}$  is broadened and drastically reduced. Since the signal of the methyl group of acetate is still intense, we attribute this effect to the interaction with the  $La^{3+}$  cations. A closer look into the  $^1H$  NMR spectrum shows also the presence of water at  $5.7\text{ ppm}$ . However, no sign of the formation of  $BMIm-2-$

ylidene or its reaction products could be found, although it must have formed at least intermediately. Although dimerization according to the Wanzlick equilibrium is not expected for this type of N-heterocyclic carbene [65,66], it cannot be excluded that the high reaction temperature allows for it.

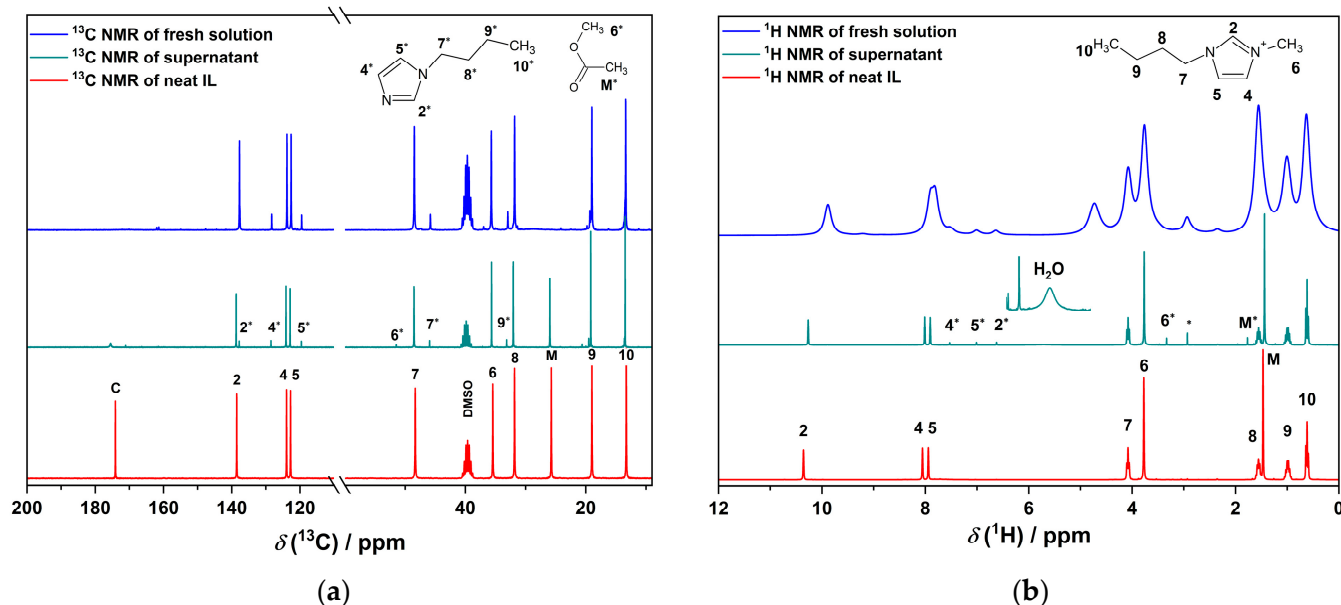


**Figure 6.** (a)  $^{13}\text{C}$  and (b)  $^1\text{H}$  NMR spectra of neat [BMIm][OAc], a freshly prepared solution of  $\text{La}_2\text{O}_3$  in [BMIm][OAc] from which no precipitation had occurred, and the supernatant of a solution from which the complex salt had precipitated and which had been stored in air for several months. The signals of [BMIm] $^+$  are assigned to the atoms at the marked positions in the structures above [26]. The asterisk sign \* indicates the decomposition product in the reacted IL. M\* and 6\* represent the methyl group of methyl acetate (decomposition product of the IL). Perdeuterated DMSO- $d_6$  was used for diluting all samples ( $^{13}\text{C}$  signal around 40 ppm).

The  $^1\text{H}$  NMR spectrum of the aged supernatant shows only weak and broadened resonances, while the  $^{13}\text{C}$  NMR signals are still sharp. We attribute this to a higher water content that has accumulated in the hygroscopic IL during the long period of exposure to the air. With a higher water content, the water signals shift to 4.7 ppm. The influence of the water concentration on the NMR signal is shown in Figure S6. Remarkably, the  $^{13}\text{C}$  NMR signals of the [BMIm] $^+$  cation are still visible, but no corresponding (carbon-based) anion can be identified.

### 3.5. Stability of the Complex Salts

The [BMIm] $_2$ [RE $_2$ (OAc) $_8$ ] complexes were obtained as single-phase products, allowing their further chemical and physical characterization. Since no decomposition was observed by visual inspections over a period of ten months, the washed crystals can be considered stable under ambient conditions. In contrast, unwashed samples are degraded to an unknown product (Figure S15).

The thermal stability in argon atmosphere of washed [BMIm] $_2$ [RE $_2$ (OAc) $_8$ ] crystals ( $RE = \text{Pr}, \text{Sm}, \text{Eu}, \text{Dy}$ ) was investigated with a differential scanning calorimeter (DSC) and thermogravimetric analysis (TGA) in the temperature range from 25 to 500  $^\circ\text{C}$ . All samples showed a two-step decomposition (Figure 7a), with a uniform onset temperature of 250  $^\circ\text{C}$  for first weight loss of 54.3%. Remarkably, the decomposition of imidazolium-based ILs was reported to start at 216  $^\circ\text{C}$  in argon atmosphere, resulting in complete evaporation of all fragments at 300  $^\circ\text{C}$  [67]. In a second step starting at about 330  $^\circ\text{C}$  and up to the maximum temperature of 500  $^\circ\text{C}$ , the mass was reduced further by 8% of the initial mass. The residual of 37.7% of the initial mass matches the

calculated mass of  $\text{Eu}_2\text{O}_2\text{CO}_3$  (37.5%), whose formation under similar conditions has been described previously [62]. The PXRD patterns of the solid residual shows a poorly crystalline material, which could be  $\text{Eu}_2\text{O}_2\text{CO}_3$  (Figure S16). The DSC thermograms of the  $[\text{BMIm}]_2[\text{Eu}_2(\text{OAc})_8]$  complex salt shows a sharp endothermic transition at  $167^\circ\text{C}$ , which indicates melting of the compound, and a broad endothermic effect starting above  $220^\circ\text{C}$ , which is associated with its decomposition (Figure 7b).

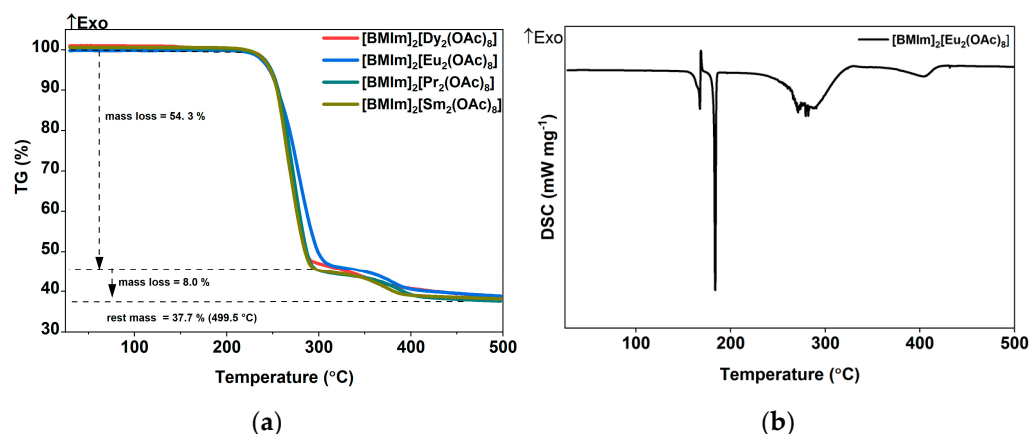


**Figure 7.** (a) TG and (b) DSC analysis of crystal structure of  $[\text{BMIm}]_2[\text{Eu}_2(\text{OAc})_8]$  during heating in a stream of argon.

### 3.6. Photoluminescence of the Eu and Sm Salts

Isolation of the homoleptic dinuclear rare-earth complexes as single-phase materials allowed us to characterize their optical properties. The UV-Vis spectra of  $[\text{BMIm}]_2[\text{Eu}_2(\text{OAc})_8]$  and  $[\text{BMIm}]_2[\text{Sm}_2(\text{OAc})_8]$  showed broad absorption bands at 214 and 261 nm (Figure 8). This absorptions correspond to  $\pi \rightarrow \pi^*$  transitions of the IL cation [68]. The absorption bands observed above 350 nm were assigned to the absorption bands of the respective rare-earth metal cations.

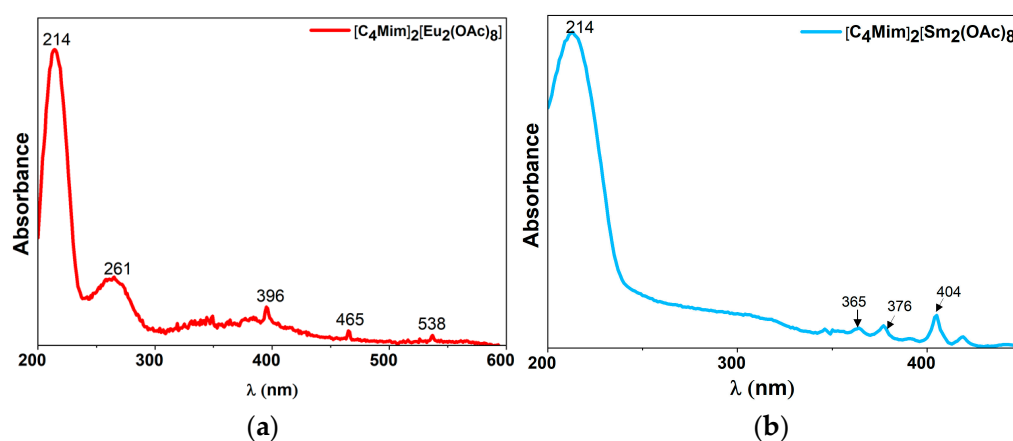


**Figure 8.** Solid-state UV-Vis spectra of (a)  $[\text{BMIm}]_2[\text{Eu}_2(\text{OAc})_8]$  and (b)  $[\text{BMIm}]_2[\text{Sm}_2(\text{OAc})_8]$ .

Under a UV lamp,  $[\text{BMIm}]_2[\text{Eu}_2(\text{OAc})_8]$  emits red light (Figure 9),  $[\text{BMIm}]_2[\text{Tb}_2(\text{OAc})_8]$  pale-green light (Figure S17), and  $[\text{BMIm}]_2[\text{Sm}_2(\text{OAc})_8]$  blue light (Figure 9). Rare-earth metal ions can show strong luminescence due to transitions involving their 4f orbitals. A narrow emission band is characteristic of metalorganic complexes [69], in which the organic ligand absorbs energy and the intramolecular transfer of this energy from  $\pi^*$  or  $n^*$  to the next closest 4f level occurs (antenna effect). The intensity of the photoluminescence depends on the energy gap between the singlet S1 and the triplet state of the ligand, and the band gap between the triplet T1 and the 4f resonance states of the metal cation. Geometry

and electronic features of the rare-earth metal complex influence the emission of spectra [7,70]. The coordination of polar molecules reduces the lifetime of the luminescence and the quantum yields. The depopulation of excited states takes place through the vibronic coupling of X-H oscillators ( $X = N, C, O$ ) [71].

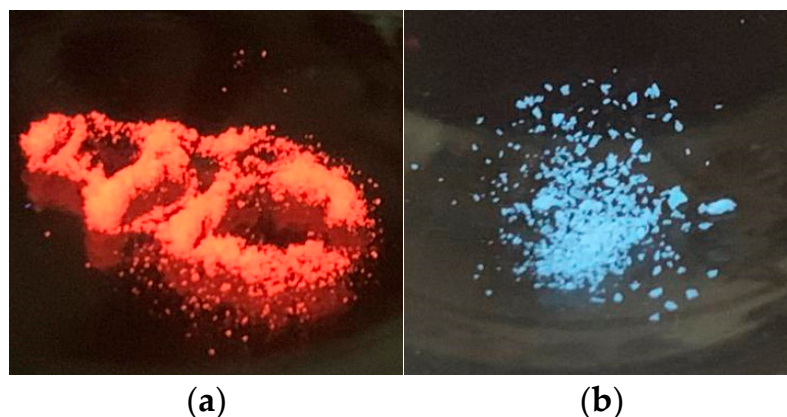


**Figure 9.** (a)  $[BMIm]_2[Eu_2(OAc)_8]$  and (b)  $[BMIm]_2[Sm_2(OAc)_8]$  under UV radiation of 312 nm.

The excitation and emission spectra were measured at room temperature for  $[BMIm]_2[Eu_2(OAc)_8]$  and  $[BMIm]_2[Sm_2(OAc)_8]$  (Figure 10). The excitation spectrum of the Eu compound was monitored at 615 nm, that is, the emission of  $Eu^{3+}$  ( $^5D_0 \rightarrow ^7F_2$ ). A series of intense and narrow lines was observed (in nm): 361, 367 ( $^7F_0 \rightarrow ^5D_4$ ), 374 ( $^7F_{0/1} \rightarrow ^5G_j$ ), 381, 385 ( $^7F_{0/1} \rightarrow ^5L_7, ^5G_j$ ), 396 ( $^7F_0 \rightarrow ^5L_6$ ), 416 ( $^7F_0 \rightarrow ^5D_3$ ), and 465 ( $^7F_0 \rightarrow ^5D_2$ ). The most prominent excitations are at 396 and 465 nm, which is similar to the excitation spectrum of  $Eu(DCA)_3$  [5]. Using the excitation at 396 nm, the emission spectrum showed lines at (in nm): 580 ( $^5D_0 \rightarrow ^7F_0$ ), 592 ( $^5D_0 \rightarrow ^7F_1$ ), 615 ( $^5D_0 \rightarrow ^7F_2$ ), and 651 ( $^5D_0 \rightarrow ^7F_3$ ), while the ( $^5D_0 \rightarrow ^7F_4$ ) transition band composed of two stark sublevels at 687 nm and 697 nm under the electric field (crystal field) were observed [72–74]. The very sharp  $^5D_0 \rightarrow ^7F_2$  transition is more intense than  $^5D_0 \rightarrow ^7F_1$ . This correlates with a  $Eu^{3+}$  cation in a distorted tricapped trigonal prism [5].

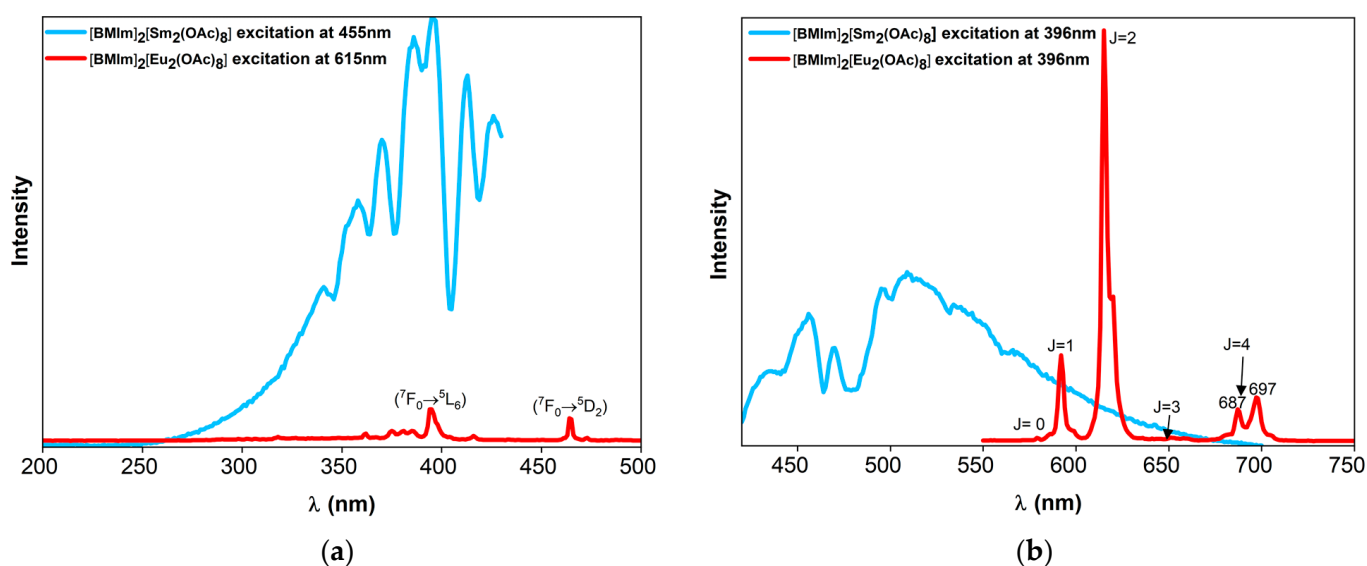


**Figure 10.** (a) Excitation and (b) emission spectra of  $[BMIm]_2[Eu_2(OAc)_8]$  and  $[BMIm]_2[Sm_2(OAc)_8]$ .

In the case of the Sm complex salt, the excitation spectra were measured at 455 nm. The entire excitation spectrum is composed of multiple broad bands, ranging from 270 to 420 nm, most likely due to inefficient energy transfer from the ligand to the  $\text{Sm}^{3+}$  cation. The maximum excitation was observed at 396 nm. The emission lines are also broad, with overlapping bands ranging from 400 to 700 nm. Commonly,  $\text{Sm}^{3+}$  emits orange-red light, but in  $[\text{BMIm}]_2[\text{Sm}_2(\text{OAc})_8]$ , the emission band is in the blue region, which cannot be explained without further investigations. Energy transfer from the imidazolium cation, which shows fluorescence between 250 and 400 nm [68], may be involved.

### 3.7. Magnetism of the Eu and Sm Salts

The rare-earth metal ions show magnetism mainly due to the interelectron repulsion and spin-orbit coupling. Strong spin-orbit coupling can also affect the degenerate state of the lanthanides and split them into  $^{2S+1}L_J$  multiplets that further split into Stark levels through the crystal field. The magnetic property of the rare-earth ions thus depends on the splitting and thermal population of the resulting states. The magnetic moment of  $[\text{BMIm}]_2[\text{Eu}_2(\text{OAc})_8]$  and  $[\text{BMIm}]_2[\text{Sm}_2(\text{OAc})_8]$  complexes were measured from 2 K to 300 K under a DC magnetic field. The temperature dependence of the molar susceptibility  $\chi_m$  (Figure 11) indicates ordinary Langevin paramagnetism for  $[\text{BMIm}]_2[\text{Sm}_2(\text{OAc})_8]$ . In contrast, for  $[\text{BMIm}]_2[\text{Eu}_2(\text{OAc})_8]$ , an increase of the magnetic susceptibility with decreasing temperature to a plateau below 100 K was observed. This behavior is consistent with Van Vleck paramagnetism [75], commonly observed for  $\text{Eu}^{3+}$ -containing compounds. The increase in  $\chi_m$  below 15 K could be explained by traces of  $\text{Eu}^{2+}$  ions, as has been observed in dinuclear europium complexes before [76].

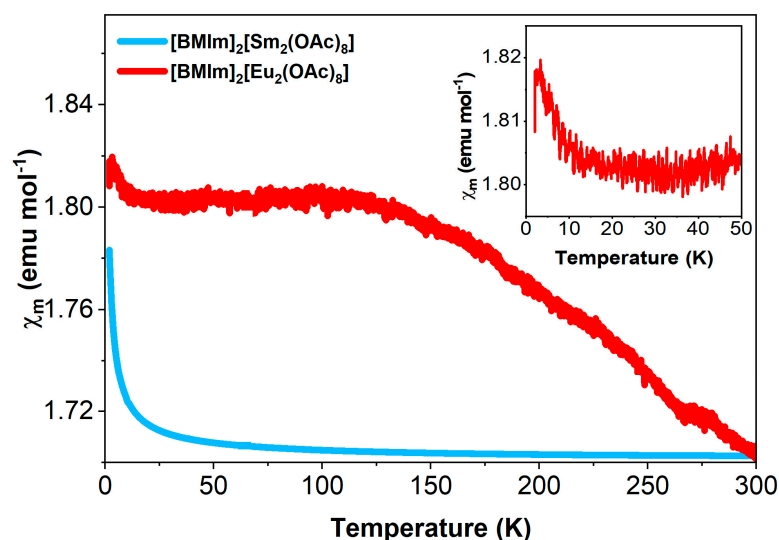


**Figure 11.** Temperature dependence of the molar susceptibility of  $[\text{BMIm}]_2[\text{Eu}_2(\text{OAc})_8]$  and  $[\text{BMIm}]_2[\text{Sm}_2(\text{OAc})_8]$ .

Generally, only the electronic ground states are occupied at low and room temperatures in the free rare-earth metal ions due to the larger-than- $k_B T$  energy splitting between the multiplets [77]. However, the  $\text{Eu}^{3+}$  ( $4f^6$ ) and  $\text{Sm}^{3+}$  ( $4f^5$ ) complexes are exceptions, as they show temperature-independent van Vleck contributions to the susceptibility. The indicative sign for this behavior is a significant curvature in the inverse susceptibility [78], which is observed for both samples (Figures S18 and S19). Due to a small energetic difference between the ground and the first excited state, the latter is substantially populated at higher temperatures [79,80]. At 300 K,  $\chi_m T$  is  $2.37 \text{ emu K mol}^{-1}$  for  $[\text{BMIm}]_2[\text{Eu}_2(\text{OAc})_8]$  and  $1.24 \text{ emu K mol}^{-1}$  for  $[\text{BMIm}]_2[\text{Sm}_2(\text{OAc})_8]$ .  $\chi_m T$  decreases continuously with decreasing temperature, which is caused by the depopulation of excited states. At low temperatures, a rigid linear change is still observed, where the

product  $\chi_m T$  remains nonzero due to the thermal population of the first excited state [79]. The effective magnetic moment per  $\text{Eu}^{3+}$  ion of  $3.02 \mu_B$  at 0.1 T in the high-temperature region decreases to  $0.15 \mu_B$  without a field using the molar susceptibility at 300 K. The effective magnetic moment per  $\text{Sm}^{3+}$  ion is  $2.40 \mu_B$  at 0.1 T. Similar values were found in the literature [58,79,81].

#### 4. Conclusions

A straightforward approach was used for the study of anhydrous dissolution of  $\text{RE}_2\text{O}_3$  in an imidazolium acetate ionic liquid. The fact that the use of water can be avoided opens up new possibilities for downstream chemistry. The proton source for the dissolution is the imidazolium cation. Abstraction of the acidic proton at the C<sup>2</sup>-atom yields an N-heterocyclic carbene (imidazole-2-ylidene). The used IL can be regenerated by reaction with acetic acid. Chloride promotes the dissolution, especially for the heavier  $\text{RE}_2\text{O}_3$  ( $\text{RE} = \text{Gd-Ho}$ ), although it is not included in the precipitating salts  $[\text{BMIm}]_2[\text{RE}_2(\text{OAc})_8]$  ( $\text{RE} = \text{La-Ho}$ ). The latter contain anhydrous, homoleptic, dinuclear complexes. The samarium and europium complex salts show blue and red photoluminescence, respectively. They are paramagnetic, with substantial van Vleck contributions.

**Supplementary Materials:** The following supporting information can be downloaded at: <https://www.mdpi.com/article/10.3390/chemistry5020094/s1>, Table S1. Results of reactions of 1 mmol  $\text{La}_2\text{O}_3$  with 10 mmol of various imidazolium or phosphonium-based ILs. Table S2. Reaction parameters of  $\text{RE}_2\text{O}_3$  used in this work. Figure S1. PXRD pattern of the white microcrystalline precipitate formed by the reaction of  $\text{La}_2\text{O}_3$  with  $[\text{BDMIm}][\text{OAc}]$  and acetic acid at room temperature together with the patterns of some reference compounds. Figure S2. Crystals of  $[\text{BMIm}]_2[\text{La}_2(\text{OAc})_8]$  formed in the absence or presence of chloride. Figure S3. PXRD diffractogram of the solid residuals after selective solution of one component from the mixtures  $\text{La}_2\text{O}_3/\text{Sc}_2\text{O}_3$ ,  $\text{La}_2\text{O}_3/\text{Lu}_2\text{O}_3$ ,  $\text{Eu}_2\text{O}_3/\text{Y}_2\text{O}_3$ , and  $\text{Eu}_2\text{O}_3/\text{CeO}_2$ . Figure S4. Pure  $[\text{BMIm}][\text{OAc}]$ , regenerated IL,  $\text{La}_2\text{O}_3$  dissolved in the IL, and decomposed IL. Figure S5. FTIR spectra of neat and regenerated  $[\text{BMIm}][\text{OAc}]$ . Figure S6.  $^1\text{H}$  NMR spectra of regenerated  $[\text{BMIm}][\text{OAc}]$  with different water content. Figure S7. Simulated and measured powder X-ray diffractogram of  $[\text{BMIm}]_2[\text{Eu}_2(\text{OAc})_8]$ . Figure S8. Transformation of  $[\text{BMIm}]_2[\text{Dy}_2(\text{OAc})_8]$ . Figure S9. PXRD diffractogram measured at 100 K of  $[\text{BMIm}]_2[\text{Dy}_2(\text{OAc})_8]$  crystals grown at room temperature or at  $5^\circ\text{C}$ . Figure S10. FTIR spectra of the IL and  $[\text{BMIm}]_2[\text{Dy}_2(\text{OAc})_8]$  crystals grown at room temperature or at  $5^\circ\text{C}$ . Table S3. Crystallographic data for  $[\text{BMIm}]_2[\text{RE}_2(\text{OAc})_8]$  salts at 100(2) K. Table S4. Metal–metal and metal–oxygen bond distances of all complexes studied in this work. Table S5. Selected interatomic distances in the Eu and La compounds, which belong to different structure types. Figure S11. Analogous sections of the structures of  $[\text{BMIm}]_2[\text{Pr}_2(\text{OAc})_8]$  and  $[\text{BMIm}]_2[\text{Ho}_2(\text{OAc})_8]$ . Figure S12. FTIR spectra of neat  $[\text{BMIm}][\text{OAc}]$ , a fresh solution of  $\text{La}_2\text{O}_3$  in the IL, and a solution with decomposed IL. Figure S13.  $^{13}\text{C}$  and  $^1\text{H}$  NMR spectra of neat  $[\text{BMIm}][\text{OAc}]$ , of a freshly prepared solution of  $\text{La}_2\text{O}_3$  in the IL, and of a solution with largely decomposed IL. Figure S14.  $^{13}\text{C}$  NMR spectrum and DEPT  $^{13}\text{C}$  NMR spectrum of a freshly prepared  $\text{La}_2\text{O}_3$  solution in  $[\text{BMIm}][\text{OAc}]$ . Figure S15. Degradation of  $[\text{BMIm}]_2[\text{Dy}_2(\text{OAc})_8]$  crystals in the reaction mixture after one month in air. Figure S16. PXRD diffractogram of  $[\text{BMIm}]_2[\text{Eu}_2(\text{OAc})_8]$  samples after DSC or after TG. Figure S17. Luminescence of  $[\text{BMIm}]_2[\text{Tb}_2(\text{OAc})_8]$  under UV light of 312 nm. Figure S18.  $\chi_m T$  and  $\chi_m^{-1}$  plots for  $[\text{BMIm}]_2[\text{Sm}_2(\text{OAc})_8]$  and  $[\text{BMIm}]_2[\text{Eu}_2(\text{OAc})_8]$ . Figure S19. Field-dependent magnetization of  $[\text{BMIm}]_2[\text{Sm}_2(\text{OAc})_8]$  and  $[\text{BMIm}]_2[\text{Eu}_2(\text{OAc})_8]$ .

**Author Contributions:** Conceptualization, M.R. and S.S.; methodology, S.S. and T.P.; validation, M.R.; investigation, S.S., T.P. and F.J.; resources, M.R.; writing—original draft preparation, S.S.; writing—review and editing, S.S., M.A.H., T.P. and M.R.; visualization, S.S. and T.P.; supervision, M.R. All authors have read and agreed to the published version of the manuscript.

**Funding:** This research received no external funding.

**Data Availability Statement:** The data presented in this study are available in the supplementary materials and available on request from the corresponding author. Crystal structure data are available at the CCDC database with the following depository numbers: [BMIm]<sub>2</sub>[La<sub>2</sub>(OAc)<sub>8</sub>] 2252467, [BMIm]<sub>2</sub>[Pr<sub>2</sub>(OAc)<sub>8</sub>] 2252287, [BMIm]<sub>2</sub>[Nd<sub>2</sub>(OAc)<sub>8</sub>] 2252437, [BMIm]<sub>2</sub>[Sm<sub>2</sub>(OAc)<sub>8</sub>] 2252450, [BMIm]<sub>2</sub>[Eu<sub>2</sub>(OAc)<sub>8</sub>] 2252260, [BMIm]<sub>2</sub>[Ho<sub>2</sub>(OAc)<sub>8</sub>] 2252271, and [BMIm]<sub>2</sub>[Tb<sub>2</sub>(OAc)<sub>8</sub>] 2252456.

**Acknowledgments:** The authors thank P. Höhn (MPI CPfS, Dresden) for the synthesis of Ce<sub>2</sub>O<sub>3</sub>. I. Kuhnert, F. Pabst, and E. Carrillo Aravena (all TU Dresden) are acknowledged for experimental support and discussions. We are grateful to A. Eychmüller and T. O. Starzynski (TU Dresden) for the photoluminescence measurement.

**Conflicts of Interest:** The authors declare no conflict of interest. The funders had no role in the design of the study; in the collection, analyses, or interpretation of data; in the writing of the manuscript; or in the decision to publish the results.

## References

1. Yan, B. *Photofunctional Rare Earth Hybrid Materials*, 1st ed.; Springer Series in Materials Science; Springer: Singapore, 2017; pp. 1–261. [\[CrossRef\]](#)
2. Peng, J.B.; Kong, X.J.; Ren, Y.P.; Long, L.-S.; Huang, R.-B.; Zheng, L.-S. Trigonal Bipyramidal Dy<sub>5</sub> Cluster Exhibiting Slow Magnetic Relaxation. *Inorg. Chem.* **2012**, *51*, 2186–2190. [\[CrossRef\]](#) [\[PubMed\]](#)
3. Nockemann, P.; Beurer, E.; Driesen, K.; Van Deun, R.; Van Hecke, K.; Van Meervelt, L.; Binnemans, K. Photostability of a Highly Luminescent Europium  $\beta$ -Diketonate Complex in Imidazolium Ionic Liquids. *Chem. Commun.* **2005**, *34*, 4354–4356. [\[CrossRef\]](#) [\[PubMed\]](#)
4. Billard, I.; Gaillard, C.; Hennig, C. Dissolution of UO<sub>2</sub>, UO<sub>3</sub> and of Some Lanthanide Oxides in BumimTf<sub>2</sub>N: Effect of Acid and Water and Formation of UO<sub>2</sub>(NO<sub>3</sub>)<sup>3-</sup>. *Dalton Trans.* **2007**, *37*, 4214–4221. [\[CrossRef\]](#)
5. Tang, S.-F.; Smetana, V.; Mishra, M.K.; Kelley, S.P.; Renier, O.; Rogers, R.D.; Mudring, A.-V. Forcing Dicyanamide Coordination to f-Elements by Dissolution in Dicyanamide-Based Ionic Liquids. *Inorg. Chem.* **2020**, *59*, 7227–7237. [\[CrossRef\]](#)
6. Tang, S.; Babai, A.; Mudring, A.-V. Europium-Based Ionic Liquids as Luminescent Soft Materials. *Angew. Chem. Int. Ed.* **2008**, *47*, 7631–7634. [\[CrossRef\]](#)
7. Prodius, D.; Mudring, A.V. Rare Earth Metal-Containing Ionic Liquids. *Coord. Chem. Rev.* **2018**, *363*, 1–16. [\[CrossRef\]](#)
8. Huang, Y.; Wang, D.; Duan, D.; Liu, J.; Cao, Y.; Peng, W. A Novel Dissolution and Synchronous Extraction of Rare Earth Elements from Bastnaesite by a Functionalized Ionic Liquid [Hbet][Tf<sub>2</sub>N]. *Minerals* **2022**, *12*, 1592. [\[CrossRef\]](#)
9. Khodakarami, M.; Alagha, L. Separation and Recovery of Rare Earth Elements Using Novel Ammonium-Based Task-Specific Ionic Liquids with Bidentate and Tridentate O-Donor Functional Groups. *Sep. Purif. Technol.* **2020**, *232*, 115952. [\[CrossRef\]](#)
10. Brown, L.C.; Hogg, J.M.; Swadźba-Kwaśny, M. Lewis Acidic Ionic Liquids. *Top. Curr. Chem.* **2017**, *375*, 78. [\[CrossRef\]](#)
11. Yao, A.; Qu, F.; Liu, Y.; Qu, G.; Lin, H.; Hu, S.; Wang, X.; Chu, T. Ionic Liquids with Polychloride Anions as Effective Oxidants for the Dissolution of UO<sub>2</sub>. *Dalton Trans.* **2019**, *48*, 16249–16257. [\[CrossRef\]](#)
12. Shahr El-Din, A.M.; Rizk, H.E.; Borai, E.H.; El Afifi, E.S.M. Selective Separation and Purification of Cerium(III) from Concentrate Liquor Associated with Monazite Processing by Cationic Exchange Resin as Adsorbent. *Chem. Pap.* **2023**, *77*, 2525–2538. [\[CrossRef\]](#)
13. Liu, T.; Ivanov, A.S. N-Oxide Ligands for Selective Separations of Lanthanides: Insights from Computation. *RSC Adv.* **2023**, *13*, 764–769. [\[CrossRef\]](#)
14. Fan, F.-L.; Qin, Z.; Cao, S.-W.; Tan, C.-M.; Huang, Q.-G.; Chen, D.-S.; Wang, J.-R.; Yin, X.-J.; Xu, C.; Feng, X.-G. Highly Efficient and Selective Dissolution Separation of Fission Products by an Ionic Liquid [Hbet][Tf<sub>2</sub>N]: A New Approach to Spent Nuclear Fuel Recycling. *J. Inorg. Chem.* **2019**, *58*, 603–609. [\[CrossRef\]](#)
15. Mohapatra, P.K.; Mahanty, B. Direct Dissolution of Metal Oxides in Ionic Liquids as a Smart Strategy for Separation: Current Status and Prospective. *Sep. Sci. Technol.* **2022**, *57*, 2792–2823. [\[CrossRef\]](#)
16. Entezari-Zarandi, A.; Larachi, F. Selective Dissolution of Rare-Earth Element Carbonates in Deep Eutectic Solvents. *J. Rare Earths* **2019**, *37*, 528–533. [\[CrossRef\]](#)
17. Li, X.; Li, Z.; Orefice, M.; Binnemans, K. Metal Recovery from Spent Samarium-Cobalt Magnets Using a Trichloride Ionic Liquid. *ACS Sustain. Chem. Eng.* **2019**, *7*, 2578–2584. [\[CrossRef\]](#)
18. Nockemann, P.; Thijs, B.; Parac-Vogt, T.N.; Van Hecke, K.; Van Meervelt, L.; Tinant, B.; Hartenbach, I.; Schleid, T.; Vu, T.N.; Minh, T.N.; et al. Carboxyl-Functionalized Task-Specific Ionic Liquids for Solubilizing Metal Oxides. *Inorg. Chem.* **2008**, *47*, 9987–9999. [\[CrossRef\]](#)
19. Quintana, A.A.; Sztapka, A.M.; Ebinuma, V.D.C.S.; Agatemor, C. Enabling Sustainable Chemistry with Ionic Liquids and Deep Eutectic Solvents: A Fad or the Future? *Angew. Chem. Int. Ed.* **2022**, *61*, e202205609. [\[CrossRef\]](#)
20. Kelley, S.P.; Smetana, V.; Emerson, S.D.; Mudring, A.V.; Rogers, R.D. Benchtop Access to Anhydrous Actinide N-Donor Coordination Complexes Using Ionic Liquids. *Chem. Commun.* **2020**, *56*, 4232–4235. [\[CrossRef\]](#)

21. Shah, S.; Pietsch, T.; Ruck, M. N-Heterocyclic Carbene-Mediated Oxidation of Copper (I) in an Imidazolium Ionic Liquid. *Z. Naturforsch. B* **2023**, *78*, 105–112. [[CrossRef](#)]
22. Flanagan, D.M.; Romanov-Michailidis, F.; White, N.A.; Rovis, T. Organocatalytic Reactions Enabled by N-Heterocyclic Carbenes. *Chem. Rev.* **2015**, *115*, 9307–9387. [[CrossRef](#)] [[PubMed](#)]
23. Liu, C.; Li, Y.; Hou, Y. Basicity Characterization of Imidazolyl Ionic Liquids and Their Application for Biomass Dissolution. *Int. J. Chem. Eng.* **2018**, *2018*, 7501659. [[CrossRef](#)]
24. Xu, A.; Guo, X.; Xu, R. Understanding the Dissolution of Cellulose in 1-Butyl-3-Methylimidazolium Acetate+DMAc Solvent. *Int. J. Biol. Macromol.* **2015**, *81*, 1000–1004. [[CrossRef](#)]
25. Liebner, F.; Patel, I.; Ebner, G.; Becker, E.; Horix, M.; Potthast, A.; Rosenau, T. Thermal Aging of 1-Alkyl-3-Methylimidazolium Ionic Liquids and Its Effect on Dissolved Cellulose. *Holzforschung* **2010**, *64*, 161–166. [[CrossRef](#)]
26. Besnard, M.; Cabaço, M.I.; Vaca Chávez, F.; Pinaud, N.; Sebastião, P.J.; Coutinho, J.A.P.; Mascetti, J.; Danten, Y. CO<sub>2</sub> in 1-Butyl-3-Methylimidazolium Acetate. 2. NMR Investigation of Chemical Reactions. *J. Phys. Chem. A* **2012**, *116*, 4890–4901. [[CrossRef](#)] [[PubMed](#)]
27. Richter, J.; Ruck, M. Dissolution of Metal Oxides in Task-Specific Ionic Liquid. *RSC Adv.* **2019**, *9*, 29699–29710. [[CrossRef](#)]
28. Orefice, M.; Binnemans, K.; Vander Hoogerstraete, T. Metal Coordination in the High-Temperature Leaching of Roasted NdFeB Magnets with the Ionic Liquid Betainium Bis(Trifluoromethylsulfonyl)Imide. *RSC Adv.* **2018**, *8*, 9299–9310. [[CrossRef](#)]
29. Lê Anh, M.; Wolff, A.; Kaiser, M.; Yogendra, S.; Weigand, J.J.; Pallmann, J.; Brunner, E.; Ruck, M.; Doert, T. Mechanistic Exploration of the Copper(I) Phosphide Synthesis in Phosphonium-Based and Phosphorus-Free Ionic Liquids. *Dalton Trans.* **2017**, *46*, 15004–15011. [[CrossRef](#)]
30. Wolff, A.; Pallmann, J.; Boucher, R.; Weiz, A.; Brunner, E.; Doert, T.; Ruck, M. Resource-Efficient High-Yield Ionothermal Synthesis of Microcrystalline Cu<sub>3</sub>-xP. *Inorg. Chem.* **2016**, *55*, 8844–8851. [[CrossRef](#)]
31. Wolff, A.; Pallmann, J.; Brunner, E.; Doert, T.; Ruck, M. On the Anion Exchange of PX<sub>3</sub> (X = Cl, Br, I) in Ionic Liquids Comprising Halide Anions. *Z. Anorg. Allg. Chem.* **2017**, *643*, 20–24. [[CrossRef](#)]
32. Getsis, A.; Balke, B.; Felser, C.; Mudring, A.V. Dysprosium-Based Ionic Liquid Crystals: Thermal, Structural, Photo- and Magnetophysical Properties. *Cryst. Growth Des.* **2009**, *9*, 4429–4437. [[CrossRef](#)]
33. Abu-Eishah, S.I.; Elsuccary, S.A.A.; Al-Attar, T.H.; Khanji, A.A.; Butt, H.P.; Mohamed, N.M. Production of 1-Butyl-3-Methylimidazolium Acetate [Bmim][Ac] Using 1-Butyl-3-Methylimidazolium Chloride [Bmim]Cl and Silver Acetate: A Kinetic Study. In *Ionic Liquids—Thermophysical Properties and Applications*, 2nd ed.; Murshed, S.M.S., Ed.; IntechOpen Limited: London, UK, 2021; pp. 1–21. [[CrossRef](#)]
34. Hamm, C.M.; Alff, L.; Albert, B. Synthesis of Microcrystalline Ce<sub>2</sub>O<sub>3</sub> and Formation of Solid Solutions between Cerium and Lanthanum Oxides. *Z. Anorg. Allg. Chem.* **2014**, *640*, 1050–1053. [[CrossRef](#)]
35. Sheldrick, G.M. *SADABS, Area-Detector Absorption Correction*; Bruker AXS Inc.: Madison, WI, USA, 2016.
36. Evans, P.R. An Introduction to Data Reduction: Space-Group Determination, Scaling and Intensity Statistics. *Acta Crystallogr. Sect. D* **2011**, *67*, 282–292. [[CrossRef](#)]
37. Sheldrick, G.M. A short history of SHELX. *Acta Crystallogr. Sect. A* **2008**, *64*, 112–122. [[CrossRef](#)]
38. OlexSys. *OLEX2*, version 1.2; OlexSys Ltd.: Durham, UK, 2014.
39. Sheldrick, G.M.; Schneider, T.R. SHELXL: High-Resolution Refinement. *Methods Enzymol.* **1997**, *277*, 319–343. [[CrossRef](#)]
40. Sheldrick, G.M. Crystal Structure Refinement with SHELXL. *Acta Crystallogr. Sect. C Struct. Chem.* **2015**, *71*, 3–8. [[CrossRef](#)]
41. Brandenburg, K. *DIAMOND 4, Crystal and Molecular Structure Visualization*, Version 4.6.8; Crystal Impact GbR: Bonn, Germany, 2022.
42. Advanced Chemistry Development, Inc. *ACChD/C+H NM Predictor and DB 2017.1.3*; Advanced Chemistry Development, Inc.: Toronto, ON, Canada, 2017; Available online: [www.acdlabs.com](http://www.acdlabs.com) (accessed on 10 July 2020).
43. *OPUS*, Version 6.5; Bruker Optik GmbH: Ettlingen, Germany, 2004.
44. Chiarotto, I.; Feroci, M.; Inesi, A. First Direct Evidence of N-Heterocyclic Carbene in BMIm Acetate Ionic Liquids. An Electrochemical and Chemical Study on the Role of Temperature. *New J. Chem.* **2017**, *41*, 7840–7843. [[CrossRef](#)]
45. Rodríguez, H.; Gurau, G.; Holbrey, J.D.; Rogers, R.D. Reaction of Elemental Chalcogens with Imidazolium Acetates to Yield Imidazole-2-Chalcogenones: Direct Evidence for Ionic Liquids as Proto-Carbenes. *Chem. Commun.* **2011**, *47*, 3222–3224. [[CrossRef](#)]
46. Shannon, R.D.; Prewitt, C.T. Effective Ionic Radii in Oxides and Fluorides. *Acta Crystallogr. Sect. B* **1969**, *25*, 925–946. [[CrossRef](#)]
47. Wendler, F.; Todt, L.N.; Meister, F. Thermostability of Imidazolium Ionic Liquids as Direct Solvents for Cellulose. *Thermochim. Acta* **2012**, *528*, 76–84. [[CrossRef](#)]
48. Kroon, M.C.; Buijs, W.; Peters, C.J.; Witkamp, G.J. Quantum Chemical Aided Prediction of the Thermal Decomposition Mechanisms and Temperatures of Ionic Liquids. *Thermochim. Acta* **2007**, *465*, 40–47. [[CrossRef](#)]
49. De Vos, N.; Maton, C.; Stevens, C.V. Electrochemical Stability of Ionic Liquids: General Influences and Degradation Mechanisms. *ChemElectroChem* **2014**, *1*, 1258–1270. [[CrossRef](#)]
50. Kirchner, B.; Blasius, J.; Alizadeh, V.; Gansäuer, A.; Hollóczki, O. Chemistry Dissolved in Ionic Liquids. A Theoretical Perspective. *J. Phys. Chem. B* **2022**, *126*, 766–777. [[CrossRef](#)] [[PubMed](#)]
51. Clough, M.T.; Geyer, K.; Hunt, P.A.; Mertes, J.; Welton, T. Thermal Decomposition of Carboxylate Ionic Liquids: Trends and Mechanisms. *Phys. Chem. Chem. Phys.* **2013**, *15*, 20480–20495. [[CrossRef](#)]

52. Fulmer, G.R.; Miller, A.J.M.; Sherden, N.H.; Gottlieb, H.E.; Nudelman, A.; Stoltz, B.M.; Bercaw, J.E.; Goldberg, K.I. NMR Chemical Shifts of Trace Impurities: Common Laboratory Solvents, Organics, and Gases in Deuterated Solvents Relevant to the Organometallic Chemist. *Organometallics* **2010**, *29*, 2176–2179. [CrossRef]
53. Socha, O.; Dračinský, M. Dimerization of Acetic Acid in the Gas Phase—NMR Experiments and Quantum-Chemical Calculations. *Molecules* **2020**, *25*, 2150. [CrossRef]
54. Zhang, Q.G.; Wang, N.N.; Yu, Z.W. The Hydrogen Bonding Interactions between the Ionic Liquid 1-Ethyl-3-Methylimidazolium Ethyl Sulfate and Water. *J. Phys. Chem. B* **2010**, *114*, 4747–4754. [CrossRef]
55. Troshenkova, S.V.; Sashina, E.S.; Novoselov, N.P.; Arndt, K.F.; Jankowsky, S. Structure of Ionic Liquids on the Basis of Imidazole and Their Mixtures with Water. *Russ. J. Gen. Chem.* **2010**, *80*, 106–111. [CrossRef]
56. Moriguchi, T.; Kawata, H.; Jalli, V. Design, Synthesis, Crystal Structure and Photoluminescence Properties of Four New Europium(III) Complexes with Fluorinated  $\beta$ -Diketone Ligand. *Cryst. Struct. Theory Appl.* **2021**, *10*, 1–13. [CrossRef]
57. Zheng, X.; Wang, M.; Li, Q. Synthesis and Luminescent Properties of Europium Complexes Covalently Bonded to Hybrid Materials Based on MCM-41 and Poly(Ionic Liquids). *Materials* **2018**, *11*, 677. [CrossRef]
58. Andruh, M.; Bakalbassis, E.; Kahn, O.; Trombe, J.C.; Porcher, P. Structure and Spectroscopic and Magnetic Properties of Rare Earth Metal(III) Derivatives with the 2-Formyl 1-4-Methyl-6-(A-(2-Pyridylethyl)Formimidoyl) Phenol Ligand. *Inorg. Chem.* **1993**, *32*, 1616–1622. [CrossRef]
59. Nockemann, P.; Thijs, B.; Lunstroot, K.; Parac-Vogt, T.N.; Görlner-Walrand, C.; Binnemans, K.; Van Hecke, K.; Van Meervelt, L.; Nikitenko, S.; Daniels, J.; et al. Speciation of Rare-Earth Metal Complexes in Ionic Liquids: A Multiple-Technique Approach. *Chem. Eur. J.* **2009**, *15*, 1449–1461. [CrossRef]
60. Marekha, B.A.; Bria, M.; Moreau, M.; De Waele, I.; Miannay, F.-A.; Smortsova, Y.; Takamuku, T.; Kalugin, O.N.; Kiselev, M.; Idrissi, A. Intermolecular Interactions in Mixtures of 1-n-Butyl-3-Methylimidazolium Acetate and Water: Insights from IR, Raman, NMR Spectroscopy and Quantum Chemistry Calculations. *J. Mol. Liq.* **2015**, *210*, 227–237. [CrossRef]
61. Nakamoto, K.; Fujita, J.; Tanaka, S.; Kobayashi, M. Infrared Spectra of Metallic Complexes. IV. Comparison of the Infrared Spectra of Unidentate and Bidentate Metallic Complexes. *J. Am. Chem. Soc.* **1957**, *79*, 4904–4908. [CrossRef]
62. Patil, K.C.; Chandrashekhar, G.V.; George, M.V.; Rao, C.N.R. Infrared Spectra and Thermal Decompositions of Metal Acetates and Dicarboxylates. *Can. J. Chem.* **1968**, *46*, 257–265. [CrossRef]
63. Trujillo-Rodríguez, M.J.; Anderson, J.L. In Situ Generation of Hydrophobic Magnetic Ionic Liquids in Stir Bar Dispersive Liquid-Liquid Microextraction Coupled with Headspace Gas Chromatography. *Talanta* **2019**, *196*, 420–428. [CrossRef]
64. Radzymińska-Lenarcik, E. Search for the Possibility of Utilizing the Differences in Complex-Forming Capacities of Alkylimidazoles for Selective Extraction of Some Metal Ions from Aqueous Solutions. *Pol. J. Chem. Technol.* **2008**, *10*, 73–78. [CrossRef]
65. Kirmse, W. The beginning of N-heterocyclic carbenes. *Angew. Chem. Int. Ed.* **2010**, *49*, 8798–8801. [CrossRef]
66. Böhm, V.P.W.; Herrmann, W.A. The Wanzlick Equilibrium. *Angew. Chem.* **2000**, *39*, 4036–4038. [CrossRef]
67. Efimova, A.; Hubrig, G.; Schmidt, P. Thermal Stability and Crystallization Behavior of Imidazolium Halide Ionic Liquids. *Thermochim. Acta* **2013**, *573*, 162–169. [CrossRef]
68. Paul, A.; Samanta, A. Optical Absorption and Fluorescence Studies on Imidazolium Ionic Liquids Comprising the Bis(Trifluoromethanesulfonyl)Imide Anion. *J. Chem. Sci.* **2006**, *118*, 335–340. [CrossRef]
69. Tilley, R.J.D. Lanthanoid Ion Color. In *Encyclopedia of Color Science and Technology*; Shamey, R., Ed.; Springer: Berlin/Heidelberg, Germany, 2020; pp. 1–10. [CrossRef]
70. Pereira, C.C.L.; Carretas, J.M.; Monteiro, B.; Leal, J.P. Luminescent Ln-Ionic Liquids beyond Europium. *Molecules* **2021**, *26*, 4834. [CrossRef] [PubMed]
71. Mudring, A.V.; Babai, A.; Arenz, S.; Giernoth, R.; Binnemans, K.; Driesen, K.; Nockemann, P. Strong Luminescence of Rare Earth Compounds in Ionic Liquids: Luminescent Properties of Lanthanide(III) Iodides in the Ionic Liquid 1-Dodecyl-3-Methylimidazolium Bis(Trifluoromethanesulfonyl)Imide. *J. Alloys Compd.* **2006**, *418*, 204–208. [CrossRef]
72. Binnemans, K. Interpretation of Europium(III) Spectra. *Coord. Chem. Rev.* **2015**, *295*, 1–45. [CrossRef]
73. Wada, S.; Kitagawa, Y.; Nakanishi, T.; Gon, M.; Tanaka, K.; Fushimi, K.; Chujo, Y.; Hasegawa, Y. Electronic Chirality Inversion of Lanthanide Complex Induced by Achiral Molecules. *Sci. Rep.* **2018**, *8*, 16395. [CrossRef]
74. Durham, D.A.; Frost, G.H.; Hart, F.A. Lanthanide Complexes-VIII Tris(2,2',6',2''-Terpyridine)Lanthanide(III)Perchlorates: Fluorescence and Structure. *J. Inorg. Nucl. Chem.* **1969**, *31*, 833–838. [CrossRef]
75. Takikawa, Y.; Ebisu, S.; Nagata, S. Van Vleck Paramagnetism of the Trivalent Eu Ions. *J. Phys. Chem. Solids* **2010**, *71*, 1592–1598. [CrossRef]
76. Matsuda, Y.; Izawa, K.; Vekhter, I. Nodal Structure of Unconventional Superconductors Probed by Angle Resolved Thermal Transport Measurements. *J. Phys. Condens. Matter* **2006**, *18*, R705–R752. [CrossRef]
77. Ferenc, W.; Cristóvão, B.; Sarzynski, J. Magnetic, Thermal and Spectroscopic Properties of Lanthanide(III) 2-(4-Chlorophenoxy) Acetates, Ln(C<sub>8</sub>H<sub>6</sub>ClO<sub>3</sub>)<sub>3</sub>.nH<sub>2</sub>O. *J. Serbian Chem. Soc.* **2013**, *78*, 1335–1349. [CrossRef]
78. Mugiraneza, S.; Hallas, A.M. Tutorial: A Beginner's Guide to Interpreting Magnetic Susceptibility Data with the Curie-Weiss Law. *Commun. Phys.* **2022**, *5*, 95. [CrossRef]
79. Farger, P.; Leuvrey, C.; Gallart, M.; Gilliot, P.; Rogez, G.; Rocha, J.; Ananias, D.; Rabu, P.; Delahaye, E. Magnetic and Luminescent Coordination Networks Based on Imidazolium Salts and Lanthanides for Sensitive Ratiometric Thermometry. *Beilstein J. Nanotechnol.* **2018**, *9*, 2775–2787. [CrossRef]

80. Fomina, I.G.; Dobrokhotova, Z.V.; Ilyukhin, A.B.; Aleksandrov, G.G.; Kazak, V.O.; Gehman, A.E.; Efimov, N.N.; Bogomyakov, A.S.; Zavorotny, Y.S.; Gerasimova, V.I.; et al. Binuclear Samarium(III) Pivalates with Chelating N-Donors: Synthesis, Structure, Thermal Behavior, Magnetic and Luminescent Properties. *Polyhedron* **2013**, *65*, 152–160. [[CrossRef](#)]
81. Wang, X.J.; Cen, Z.M.; Ni, Q.L.; Jiang, X.F.; Lian, H.C.; Gui, L.C.; Zuo, H.H.; Wang, Z.Y. Synthesis, Structures and Properties of Functional 2-D Lanthanide Coordination Polymers  $[\text{Ln}_2(\text{Dpa})_2(\text{C}_2\text{O}_4)_2(\text{H}_2\text{O})_2]_n$  (Dpa = 2,2'-(2-Methylbenzimidazolium-1,3-Diyl)Diacetate,  $\text{C}_2\text{O}_4^{2-}$  = Oxalate, Ln = Nd, Eu, Gd, Tb). *Cryst. Growth Des.* **2010**, *10*, 2960–2968. [[CrossRef](#)]

**Disclaimer/Publisher's Note:** The statements, opinions and data contained in all publications are solely those of the individual author(s) and contributor(s) and not of MDPI and/or the editor(s). MDPI and/or the editor(s) disclaim responsibility for any injury to people or property resulting from any ideas, methods, instructions or products referred to in the content.